ACS OMEGA

Open Access

http://pubs.acs.org/journal/acsodf

Article

Nanoporous Carbon-Supported Bimetallic (Ni, Cu, and Fe)-Mo Catalysts for Partial Hydrogenation of Biodiesel

Dolrudee Jaruwat, Napat Kaewtrakulchai, Siwat Siriorarnroj, Atthapon Srifa, Worapon Kiatkittipong, Sumittra Charojrochkul, Masayoshi Fuji, Apiluck Eiad-Ua,* and Suttichai Assabumrungrat

Cite This: *ACS Omega* 2024, 9, 42329−42342

Read Online

ACCESS | Metrics & More | Article Recommendations

ABSTRACT: Upgrading biodiesel or hydrogenated fatty acid methyl esters (H-FAMEs) by partial hydrogenation is a second-generation biofuel with high specific fuel characteristics, such as superior cold flow properties, higher oxidative stability, and lower hazardous gas emissions, allowing this biofuel to provide excellent fuel properties, over conventional biodiesel. This study assessed the potential of using nanoporous carbon produced from cattail leaves (CL) as an alternative catalyst support. We synthesized various catalysts including monometallic Mo/NPC, Ni/NPC, Ce/NPC, and Fe/NPC catalysts, as well as bimetallic molybdenum-based catalysts doped with nickel, copper, or iron for the partial hydrogenation of soybean biodiesel. The NPC support demonstrated a surface area (S_{BET}) of approximately 1,323 m^2g^{-1}, which greatly increases the catalytic activity through the efficient dispersion of catalyst active sites. The partial hydrogenation reaction of soybean FAME over the MoNi/NPC catalyst obtained the highest catalytic activity with enhanced oxidation stability from 3 to 14 h, and the cloud point and pour point increased from 2 to 13 °C and −1 to 10 °C, respectively. Hence, the selection of catalysts is crucial due to their impact on the feasibility of the process and its economic viability. This article focuses on highlighting the effectiveness of a highly promising catalyst for partial hydrogenation as well as examining the variables that influence the primary reaction pathway.

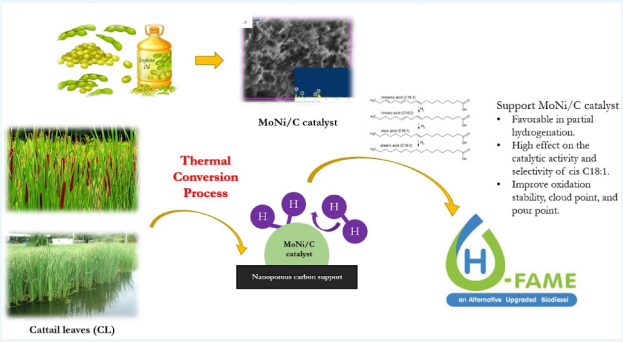

1. INTRODUCTION

Nowadays, energy consumption has greatly expanded, especially in transportation and industry. Fossil fuels such as diesel have encountered problems with incomplete combustion engines, resulting in vehicle pollutants i.e., particulate matter (PM), hydrocarbon (HC), carbon dioxide (CO_2), carbon monoxide (CO), and nitrogen oxides (NO_x).[1] They are hugely responsible for air quality deterioration. Around 22% of greenhouse gas is released from the transport sector. The International Energy Agency (IEA) estimates that, there will be 8.6 billion tons of carbon dioxide releasing into the atmosphere from 2020 to 2035.[2] Biodiesel is an alternative energy source that is obtained from biomass. The fossil diesel consumption can be reduced by blending it with biodiesel. Currently, 7% biodiesel blending (B7) for diesel engines has been accepted by car manufacturers. Several countries have aimed to increase the proportion of biodiesel blending up to 20% but limitations might be from fuel properties such as viscosity, density, calorific value, flash point, cloud point, pour point, carbon residue, and oxidation stability. The fuel properties of vegetable oil are different from diesel fuel because of molecular structure and composition.[3] Polyunsaturated fatty acid methyl esters (FAMEs) are present in the composite of the feedstock during transesterification. If biodiesel contains high polyunsaturated FAMEs, the biodiesel is unable to be stored for a long time, which affects the overall quality of biodiesel.[4] Acidity and viscosity are the causes of corrosion and engine parts clogging. Therefore, the hydrogenation reaction of unsaturated fatty acids could improve the oxidation stability of biodiesel. The complete hydrogenation operates under severe conditions, causing poor cold flow properties. The high number of saturated FAMEs exhibits a negative effect on fuel blockage in the fuel systems of vehicles. Therefore, mild reactions might convert polyunsaturated FAMEs to monounsaturated FAMEs without affecting the cold flow properties. It is difficult to control the activity and selectivity of the desired product in which catalysts can enhance the forward reactions to obtain the saturated FAME.[5]

Received: June 3, 2024
Revised: September 16, 2024
Accepted: September 24, 2024
Published: October 3, 2024

Noble metals (Pd, Pt, and Rh) are generally used as catalysts for partial hydrogenation. Although Pd is the most active catalyst compared to Rh, Ni, and Pt, it is also expensive and exhibits higher selectivity toward C18:0 and trans-isomers with a high melting point. Transition metal catalysts such as Mn, Fe, Co, Ni, Cu, and Zn have been employed for partial hydrogenation because of their lower cost.[6,7] However, Ni has limited catalytic activity compared to noble metals and operates under high-pressure H_2. Therefore, there are several bimetallic catalysts with the second promoter, which could improve the electronic structure and geometry resulting in high catalytic activity. It is recognized that bimetallic surfaces usually show unique properties which did not appear on both monometallic surfaces. Bimetallic catalysts can improve both activity and selectivity of cis-isomer content in H-FAME. Bimetallic catalyst is attractive in modified catalysts such as PdPt, PtNi, NiAg and PdMo, which could enhance oxidation stability while maintaining cold flow properties.[8] Moreover, the type of catalyst is important to convert the monosaturated FAME. Another important factor is the support material in which inorganic supports such as zeolite, silica, and alumina are commonly used. Although the acidity of the support material promotes catalytic activity, it also causes catalyst deactivation. Acidic supports enhance the formation of coking on the catalyst, because it is sensitive to carbon compounds in biodiesel.

As mentioned above, the catalyst has a short lifetime and requires regeneration. Besides, the inorganic support has a low surface area and a small pore size, which affects the dispersion of the active phase and the mass transfer of oil molecules. Porous carbon is one of the materials used as a catalyst support for partial hydrogenation because of its high surface area and large pore diameter for metal distribution and biodiesel yield.[9] The advantages of porous carbon are low coke formation, thermal stability, biodegradable materials, cost-effectiveness, and raw material availability such as coconut shell, bagasse, and rice husk.[10] An application of porous carbon produced from biomass as a catalyst support for partial hydrogenation of soybean biodiesel to H-FAME is a promising alternative compared with other supports.

Therefore, the novelty of this study is to synthesize nanoporous carbon (NPC) from cattail leaves, and the obtained NPC was applied as a catalyst support for the partial hydrogenation of soybean biodiesel to hydrogenated fatty acid methyl esters (H-FAMEs). This concept is significantly attractive because it follows the concept of a bio- and circular economy model by turning weed waste into a high value-added product. The cattail leaf-derived nanoporous carbon was synthesized via a hydrothermal technique combined with chemical activation at different temperatures in the range of 500−900 °C. The properties of nanoporous carbon were investigated using FTIR, SEM, nitrogen-sorption analysis, proximate and ultimate analyses, and CHNO. Then, the studied catalysts supported on NPC were synthesized by a wet impregnationmethod. The catalysts were characterized using XRD, SEM-EDS, nitrogen-sorption, H_2-chemisorption, and H_2−temperature-program-reduction (TPD). Moreover, a continuous flow trickle-bed reactor was used to examine the catalytic activity including the conversion of polyunsaturated FAMEs and selectivity of cis-isomer in partial hydrogenation. Finally, the properties of H-FAMEs such as oxidation stability, cloud point, and pour point were further evaluated.

2. MATERIALS AND METHODS

2.1. Materials. Cattail leaves (*Typha angustifolia*) collected from local wetland areas in Ladkrabang, Bangkok, Thailand were chosen as a feedstock for synthesizing nanoporous carbons. The chemical compositions of cellulose and lignin were approximately 38.5% and 12.8%, respectively. Soybean oil was obtained from Thai Vegetable Oil PLC.

2.2. Cattail Leaf-Derived NanoPorous Carbon (NPC). The NPC was prepared using hydrothermal carbonization; the dried cattail leaves (CL) were crushed to powder and sieved to a particle size of 2 μm. The ratio of raw feedstock to liquid media was about 1:2 (dried CL, g: deionized water, mL). Additionally, hydrochar (HC) was dried to eliminate moisture in an oven at 90 °C for 12 h. Furthermore, 10 g of dried HC was stirred at 100 rpm at 80 °C in 100 mL of 2, 4, and 6 M sulfuric acid (H_2SO_4), phosphoric acid (H_3PO_4), potassium hydroxide (KOH), and sodium hydroxide (NaOH), respectively. Then, the mixture of HC was filtered and dried. The dried HC were carbonized in a horizontal tube furnace at 500, 700, and 900 °C for 2 h under a N_2 flow of 100 mL/min at a heating rate of 10 °C/min. Finally, the samples were washed with 0.5 M HCl and distilled water several times until neutralization of the sample followed by overnight drying at 90 °C to obtain the nanoporous carbon.

2.3. Catalyst Preparation. Ammonium molybdate $[(NH_4)_6Mo_7O_{24}{\cdot}4H_2O]$, nickel(II) nitrate $[Ni(NO_3)_2{\cdot}6H_2O]$, copper(II) nitrate hexahydrate $[(Cu(NO_3)_2{\cdot}6H_2O)]$, and iron(III) nitrate hexahydrate $[(Fe(NO_3)_3{\cdot}9H_2O)]$, purity $'' \geq ''$ 98%, were used as precursors of metals. The catalyst was synthesized by wet impregnation and reflux of 50 mL. The constant metal loading was totally fixed at 10 wt % for monometallic and bimetallic catalysts. For bimetallic catalysts, the Mo-based catalysts were synthesized with various metal loading ratios of 2.5:7.5, 5:5, and 7.5:2:5 (metals(Ni, Cu, Fe):Mo, w/w). The corresponding metal precursor solution was mixed with 5 g of nanoporous carbon at 60 °C and dried using a rotary evaporator under a vacuum until complete evaporation. Then, the impregnated samples were pretreated at 500 °C for 3 h under N_2 flow to preserve them for further catalytic partial hydrogenation. Moreover, the Pd/NPC catalyst with 1% metal loading was investigated to compare the catalyst performance with the synthesized alternative catalysts in the partial hydrogenation of soybean biodiesel. Before the catalytic test is conducted, it is essential to reduce the produced catalysts with hydrogen to obtain the desired fresh metallic catalysts.

2.4. Characterization. Proximate analysis was usually used for characterizing the composition of nanoporous carbon and biomass by the thermogravimetric method. The ultimate analysis was used to estimate the composition of nanoporous carbon, either solid or gaseous, which is expressed in the form of proportions of chemical element determined by using a CHN elemental analyzer (CHNS628 series). The functional group on the surface of NPC was studied by Fourier transform infrared spectroscopy (FTIR). Moreover, the surface morphology of the NPC was observed using a scanning electron microscope (SEM, Zeiss EVO MA10). Moreover, energy-dispersive spectrometry (EDS) contributed information on the distribution of elements in the catalyst including atomic ratios of elements. The porosity and pore structure of activated carbon were measured by nitrogen adsorption−desorption at −196 °C using a Quantachrome Autosorp iQ−MP−XR. The

https://doi.org/10.1021/acsomega.4c05207
ACS Omega 2024, 9, 42329−42342

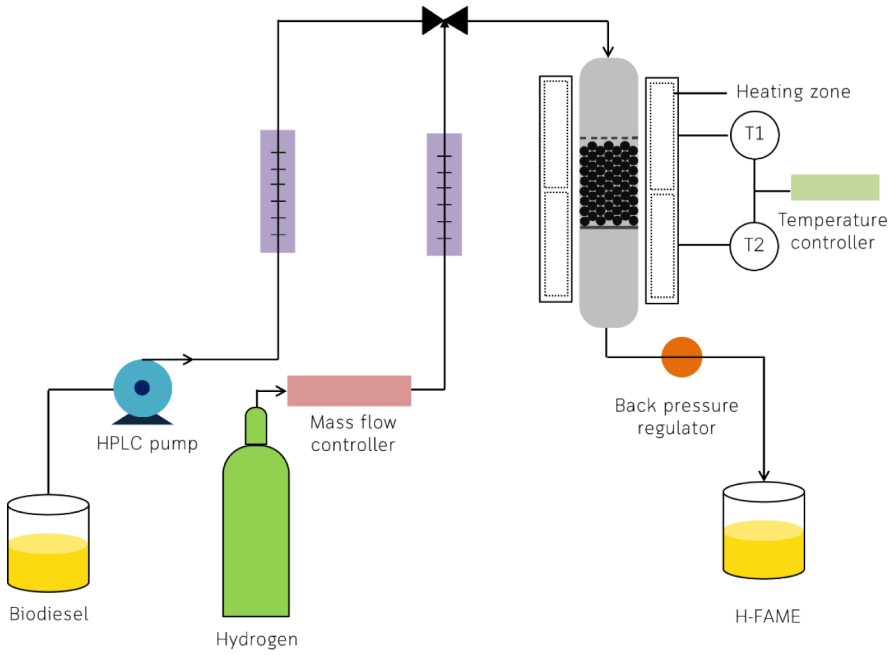

Figure 1. Schematic diagram of the continuous trickle-bed reactor.

Brunauer−Emmett−Teller (BET) method was applied for the determination of the BET surface area (S_{BET}). Simultaneously, the pore size distribution was analyzed using a density functional theory (DFT) model, while the micropore volume (V_{mic}) was determined using the t-plot model. The total pore volume (V_{total}) was evaluated using the condensation of liquid nitrogen at a relative pressure of 0.99. The mesopore volume (V_{mes}) was calculated by subtracting the micropore volume from the total pore volume.[11] The X-ray diffraction (XRD, Rigaku Smart Lab) was used to investigate phases, crystal structures, and crystallite sizes. H_2 temperature-programmed reduction (H_2-TPR, TP-5000-II) was used to investigate the reducibility of catalyst using a thermal conductivity detector (TCD). Metal dispersion of catalysts was performed using an Ohkura Riken R6015-S, and the amount of CO adsorption was calculated from the difference between the amount detected at the outlet and the total amounts of CO injected at the inlet. The catalyst particle size and metal dispersion were calculated using the cubic particle model.[12]

2.5. Partial Hydrogenation of Soybean Biodiesel. Soybean oil obtained from Thai Vegetable Oil PLC was used as a biodiesel feedstock for the transesterification reaction. The reaction was carried out in a 500 mL three-necked round-bottomed flask connected to the methanol condenser using 100 mL of soybean oil. Soybean oil was heated to 60 °C in a heating mantle. Potassium hydroxide (1% w/w of oil) was stirred in methanol with a 9:1 methanol to oil molar ratio until it dissolved completely. Then, the mixture was added to the three-necked round-bottomed flask at 60 °C while stirring at 500 rpm for 1 h. After the reaction had been completed, the reactor was cooled to room temperature. The mixture was placed in a separatory funnel until the phase separation between biodiesel and glycerol was observed, where the lower phase of glycerol was eliminated. The obtained product was washed with distilled water at 60 °C several times to remove the excess methanol, soap, and potassium hydroxide until the product was totally neutralized. Finally, the water in the product was adsorbed by anhydrous magnesium sulfate ($MgSO_4$) to obtain a soybean FAME for partial hydrogenation.

A partial hydrogenation of soybean FAMEs was conducted in a custom-made continuous-flow trickle-bed reactor constructed by using stainless steel 316, with a 7 mm I.D. and 300 mm length. A schematic diagram of the experimental apparatus is displayed in Figure 1. The reactor system comprised a feed unit, reaction test unit, and product separation unit. The heating system was controlled using a K-type temperature controller in an electrical tube furnace, while the pressure of the reactor was controlled using a back-pressure regulator. The feed rate was controlled using an HPLC pump and the gas flow rate was used to control the mass flow of gases for the reaction. Technically, the catalysts were packed in the middle of the reactor tube at the uniform temperature distribution zone. 1 g of the catalyst was packed inside the reactor and reduced under a H_2 flow of 50 mL/min at 450 °C for Cu/NPC and MoCu/NPC catalysts and 650 °C for other catalysts with a reduction time of 3 h. After reduction, the reaction mixture was cooled to the desired reaction temperatures between 80 and 140 °C. The reactor was pressurized to 0.4 MPa H_2 pressure. Then, the soybean biodiesel was fed through the reactor using an HPLC pump with a flow rate of 40 g/h. The flow rate of H_2 was controlled using a mass flow controller at 100 mL/min. The liquid product was collected every 1 h for analysis.

2.6. Biodiesel Analysis. Compositions of biodiesel before and after the partial hydrogenation reaction were investigated using a gas chromatograph installed with a flame ionization detector (GC-2010, Shimadzu) and a capillary column (HP-88, 100 m × 0.25 mm × 0.2 μm). Helium was employed as a carrier gas with a flow rate of 53.8 mL/min. Samples of 1 μL were injected into an oven at 170 °C. After 40 min, the injector temperature was increased to 230 °C with a rate of 4 °C/min. The detector temperature was fixed at 250 °C with a split ratio of 50 and maintained for 2.5 min with a total analysis time of 65 min. FAME composition was identified with reference to the retention time. The quantity of the FAME composition is defined and calculated from the ratio of the area under the

https://doi.org/10.1021/acsomega.4c05207
ACS Omega 2024, 9, 42329−42342

Table 1. Ultimate and Proximate Analysis of Cattail Leaves, Hydrochar, and Nanoporous Carbon with Alkaline Activation

	Ultimate analysis (wt%)				Proximate analysis (wt%)			
Sample	C	H	N	O*	FC%[a]	VM%[b]	M%[c]	A%[d]
CL	39.95	4.46	1.74	53.85	20.31	75.90	1.58	2.21
HC	45.45	4.40	1.83	48.32	33.28	62.31	1.63	2.78
KO500−4	58.86	4.69	1.69	34.76	72.89	19.97	1.01	6.13
KO700−4	69.19	4.18	1.31	25.32	78.64	13.67	1.43	6.26
KO900−4	86.35	4.67	1.64	7.34	81.18	10.41	1.59	6.82
KO900−2	77.61	4.26	1.49	16.64	79.84	13.98	1.29	4.89

[a]FC% is fixed carbon (%); FC (%) = 100 − VM% − M% − A%. [b]VM% is volatile matter (%). [c]M% is moisture. [d]A% is Ash (%).

maximum peak. In addition, the oxidation stability of the product is analyzed by measuring the induction period (IP) using a Metrohm 743 Rancimat.

3. RESULTS AND DISCUSSION

3.1. Synthesis of Nanoporous Carbon (NPC). Table 1 shows the chemical compositions of cattail leaves (CL) and hydrochar (HC). The carbon content of HC increased from 39.95 to 45.45 wt % while the oxygen and hydrogen content decreased from 53.85 to 48.32 wt % and 4.46 to 4.40 wt %, respectively. Also, the elemental composition of CL porous carbon is depicted in Table 1. During activation, the noncarbon contents (H, O, and N) were slightly eliminated in gases formed by devolatilization. The loss of the O content corresponded to the release of volatile matter. On the contrary, the higher activation temperature enhanced the C content and fixed carbon in the aromatic structure. H content was slightly decreased via dehydrogenation reaction, while the O content was significantly reduced via deoxygenation. At 900 °C, the observed O content was reduced to 7.34 wt % while C content was increased to 86.35 wt %. The findings confirm that the excess concentration (KO900−6) reduced the fixed carbon, because the alkaline metal residues became ash after combustion. The remaining ash consists of MgO, CaO, K_2O, and SO_3, which blocked pores and reduced the carbon yield. Although the lower concentration (KO900−2) might produce a small amount of ash, it contains high volatile matter and low fixed carbon content. Thus, KO900−4 indicates 81.18 wt % of fixed carbon while retaining 10.41 wt % of volatile matter. The above experiments have concluded that the activated carbon prepared with 4 M KOH at 900 °C was suitable as a support material due to its greatest surface area and porosity.

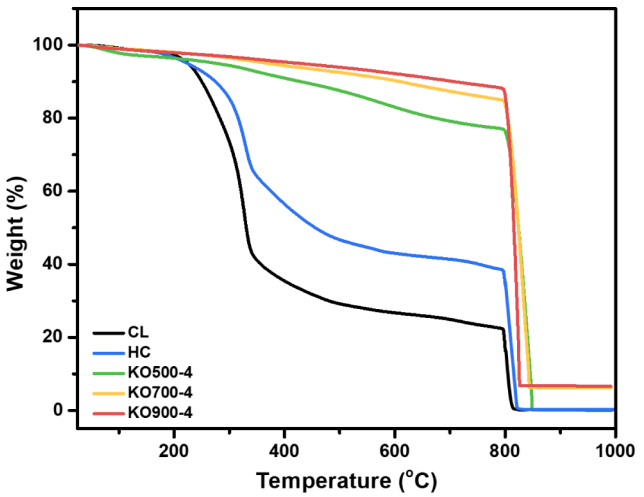

Figure 2. Thermalgravimetric analyses of nanoporous carbon.

Thermogravimetric analyses of CL and HC are presented in Figure 2. In the first step, moisture content and light mass volatiles of all samples evaporated at 30−150 °C due to dehydration. Hemicellulose with an amorphous structure could be decomposed easily at 200−280 °C, which releases compounds such as CH_4, H_2O, CO, CO_2, SO_2, and SO_3.[13,14] The loss of volatile matter (VM) was increased the fixed carbon (FC) from 20.31 to 33.28, while the moisture was slightly decreased at 110 °C, which would be further investigated using Fourier transform infrared (FT-IR). Moreover, Figure 2 shows the thermogravimetric analysis of activated carbon obtained by KOH activation in the temperature range of 500−900 °C. The TGA curves significantly decreased between 30 and 150 °C because moisture content and light mass volatiles disappeared through a dehydration reaction, while the high mass volatiles degraded toward CO, CO_2, and some hydrocarbons (CH_4, C_2H_4, and C_2H_6) at 200−500 °C. The weight loss of KO500−4 was higher than that of KO700−4 and KO900−4 because cellulose and lignin remained in the structure after activation at 500 °C. After turning off the nitrogen gas at 800 °C, the curve of all samples rapidly decreased. The fixed carbon completely decomposed, which became ash (MgO, CaO, K_2O, and SO_3) via an oxidation reaction. These results show that KO900−4 contains the highest fixed carbon and the lowest volatile content. Consequently, the high activation temperature remarkably affected the loss of volatile content and the rise of fixed carbon.

FTIR spectra of CL and HC are exhibited in Figure 3a. The main compositions of CL were hemicellulose, cellulose, and lignin around 8.7%, 63%, and 9.6%, respectively. The symmetrical C−O stretching at 1290−950 cm^{-1} greatly disappeared because the amorphous structure of hemicellulose significantly decomposed at 180−200 °C. The intensity of O−H stretching was slightly reduced (3680−3000 cm^{-1}) because orderly arranged cellulose was initially decomposed at 230 °C.[15] Moreover, the remaining C═C and C═O stretching (1600 and 1700 cm^{-1}) indicated the carbonyl and aromatic ring, in which the lignin structure was hardly decomposed during the hydrothermal process. The surface morphology of CL in Figure 3a reveals that CL was a smooth fiber. Figure 3b shows the FTIR spectra of activated carbon with sulfuric acid, phosphoric acid, sodium hydroxide, and potassium hydroxide activations. All samples show the disappearance of broadband between 1290 and 950 cm^{-1} attributed to the C−O stretching, which indicate the decomposition of hemicellulose. The disintegration of peak located at 3680−3000 cm^{-1} ascribing to −OH stretching is because cellulose has been completely decomposed after the activation process. HP500−4 sample shows peaks at 1114 and 1220 cm^{-1} which are attributed to the

https://doi.org/10.1021/acsomega.4c05207
ACS Omega 2024, 9, 42329−42342

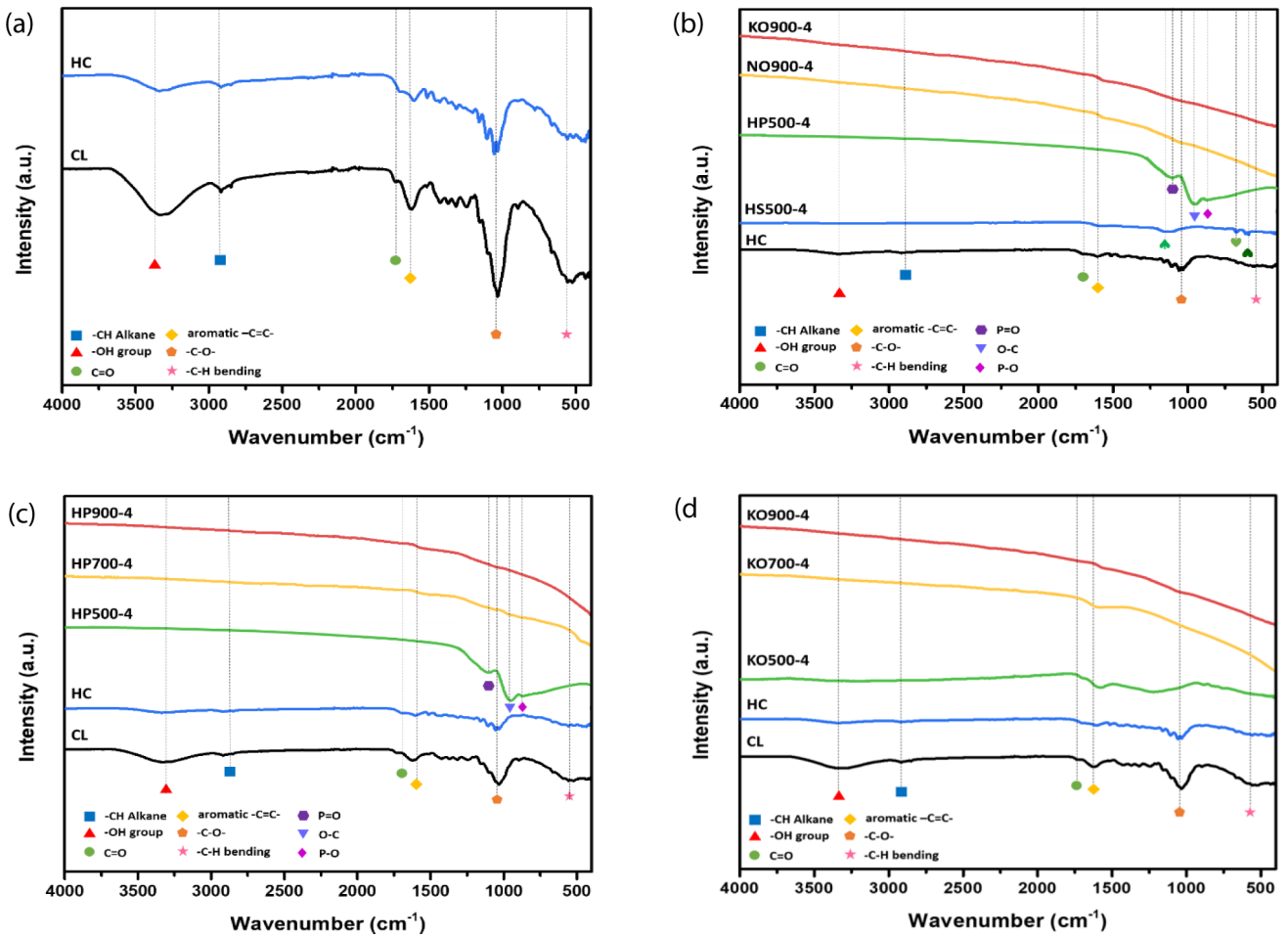

Figure 3. (a) FTIR spectra of CL and HC, (b) FTIR spectra of nanoporous carbon, (c) FTIR spectra of activated carbon with acid activation, and (d) FTIR spectra of nanoporous carbon with alkaline activation.

Table 2. Textural Properties of Nanoporous Carbon

Sample	S_{BET} (m^2g^{-1})	Pore size diameter (nm)	V_{total} (cm^3g^{-1})	V_{micro} (cm^3g^{-1})	V_{meso} (cm^3g^{-1})	V_{micro} (%)	V_{meso} (%)
KO900−4	1323.58	2.780	0.783	0.721	0.062	92.08	7.92
NO900−4	1219.61	2.596	0.672	0.428	0.244	63.69	36.30
HS500−4	429.64	1.006	0.267	0.146	0.120	54.68	45.32
HP500−4	845.33	1.152	0.454	0.166	0.333	36.56	63.44

P═O and O−C stretching vibration in the P−O−C (aromatic) linkage and P═OOH in phosphate ester. The peak at 1080 cm^{-1} indicates the appearance of the P−O−P of polyphosphate, while phosphoric acid penetrates among the formation of phosphate esters on cellulose side-chains and cross-linking.[16] These results indicate that phosphoric acid functions as both an acid catalyst for bond cleavage and for the formation of cross-links via cyclization and condensation reactions. Furthermore, cross-link biopolymer fragments connect with phosphate and a polyphosphate bridge. Moreover, the disappearance of −OH stretching (3680−3000 cm^{-1}) indicates that phosphoric acid promotes the decomposition of cellulose via dehydration reaction.[17] NO900−4 and KO900−5 appear at a similar peak, which makes it difficult to describe the difference in the intensity. Both samples activated by KOH and NaOH illustrate the peak at 1600 cm^{-1}, which is attributed to the C═C stretching vibration of an aromatic ring structure. The peak at 1700 cm^{-1} is ascribed to the C═O stretching vibration as indicated in the carbonyl, ester, or carboxyl group. These peaks remained on the surface of sample after activation at 900 °C, at which they were slightly decomposed.

After the hydrothermal process, Figure 3b confirms that the fibers shrank because the bonds of hemicellulose were broken via a hydrolysis reaction, while cellulose also remained in the fiber. Therefore, the hydrothermal process significantly broke the hemicellulose structure.[18,19] Table 2 confirms that the surface area and mesopore volume of KO900−4 were 1323.58 m^2/g and 92.1%, respectively. Therefore, a high temperature was important to develop the porosity via KOH activation. In contrast, H_3PO_4 activation was discouraged when increasing the activation temperature. Figure 3c shows the functional groups of activated carbon (HP500−4, HP700−4, and HP900−4) obtained from different activating temperatures with phosphoric acid. During activation in the range of 150−500 °C, the peak of C−O stretching at 1290−950 cm^{-1} disappeared because glycosidic bond of hemicellulose was hydrolyzed by acid catalyst. Meanwhile, aryl-ether bonds in lignin were cleaved according to a reduction of O−H

https://doi.org/10.1021/acsomega.4c05207
ACS Omega 2024, 9, 42329−42342

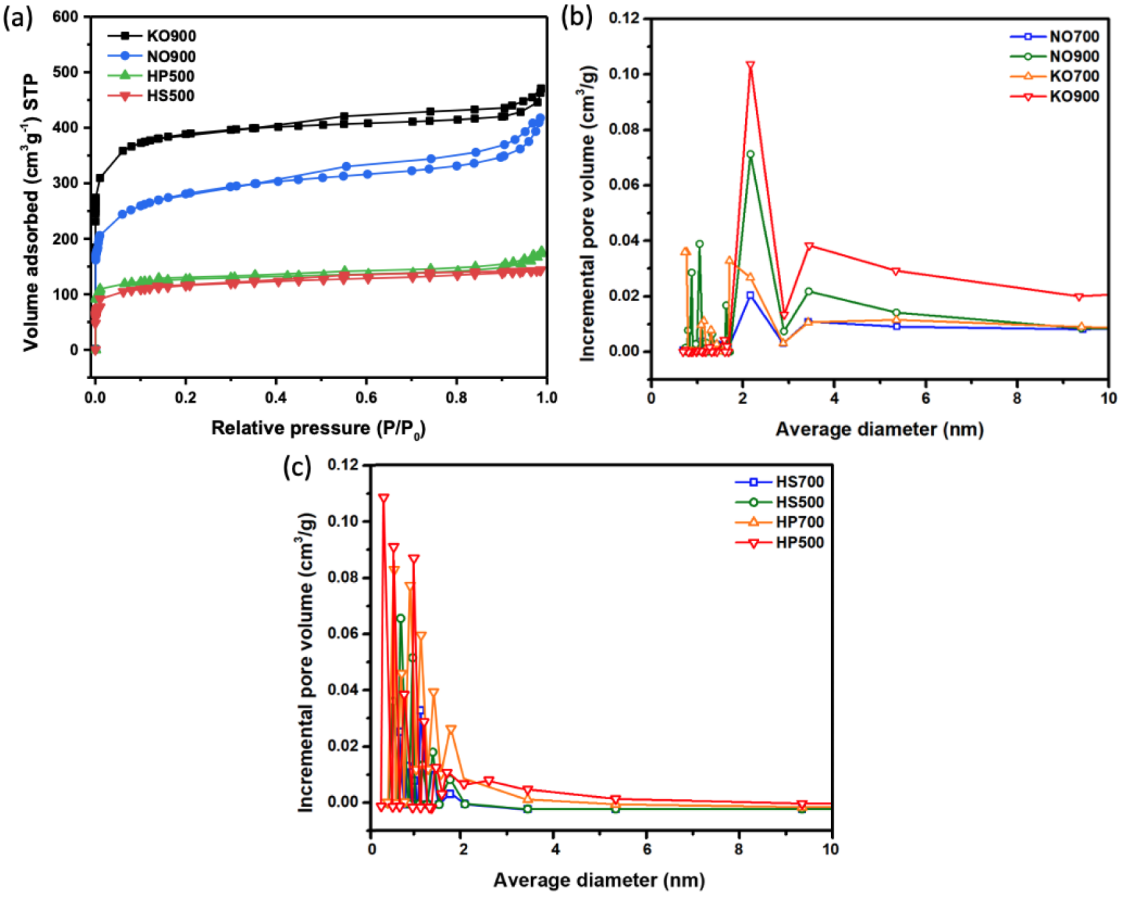

Figure 4. (a) Adsorption isotherms of N_2 on nanoporous carbon at 77 K, (b) pore size distribution of nanoporous carbon with alkaline activation, and (c) pore size distribution of nanoporous carbon with acid activation.

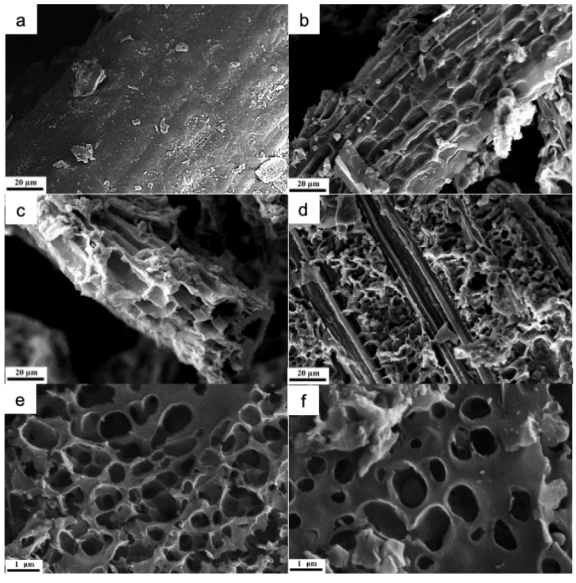

Figure 5. SEM images of (a) CL, (b) HC, (c) HS500−4, (d) HP500−4, (e) KO900−4, and (f) NO900−4.

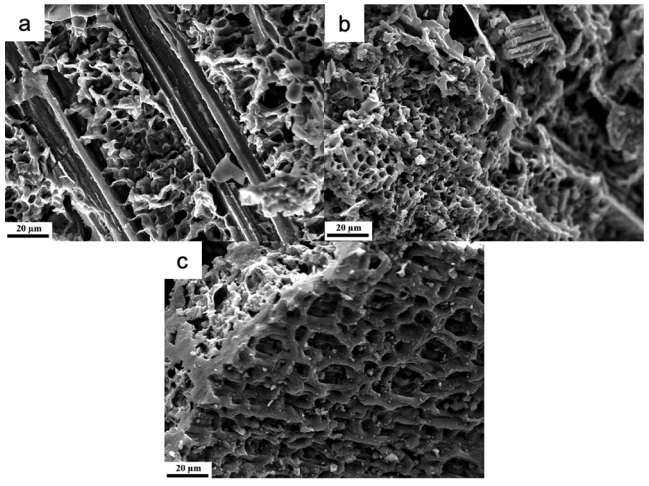

Figure 6. SEM of nanoporous carbons of (a) KO500−4, (b) KO700−4, and (c) KO900−4.

stretching at 3680−3000 cm^{-1}. These cleavage bonds released volatiles of CO_2, CO and CH_4. The formation of phosphate groups and polyphosphate esters including polyaromatics was described earlier. At above 500 °C, the FTIR spectra revealed a decrease in the intensity of the peak attributed to phosphate esters (1080 cm^{-1}). The decomposition of phosphate esters at high temperature resulted in the break of the aromatic cluster via cyclization and condensation reactions, which disappeared in the broadband of P═O, O−C stretching vibration in P−O−C (1114 and 1220 cm^{-1}). These results indicated a decrease in the porosity of nanoporous carbon, because of the structure contraction. Figure 3d shows the functional group of activated carbon (KO500−4, KO700−4, and KO900−4) obtained from an activation at 500−900 °C with potassium hydroxide. After KOH activation at 500 °C, it remained a

https://doi.org/10.1021/acsomega.4c05207
ACS Omega 2024, 9, 42329−42342

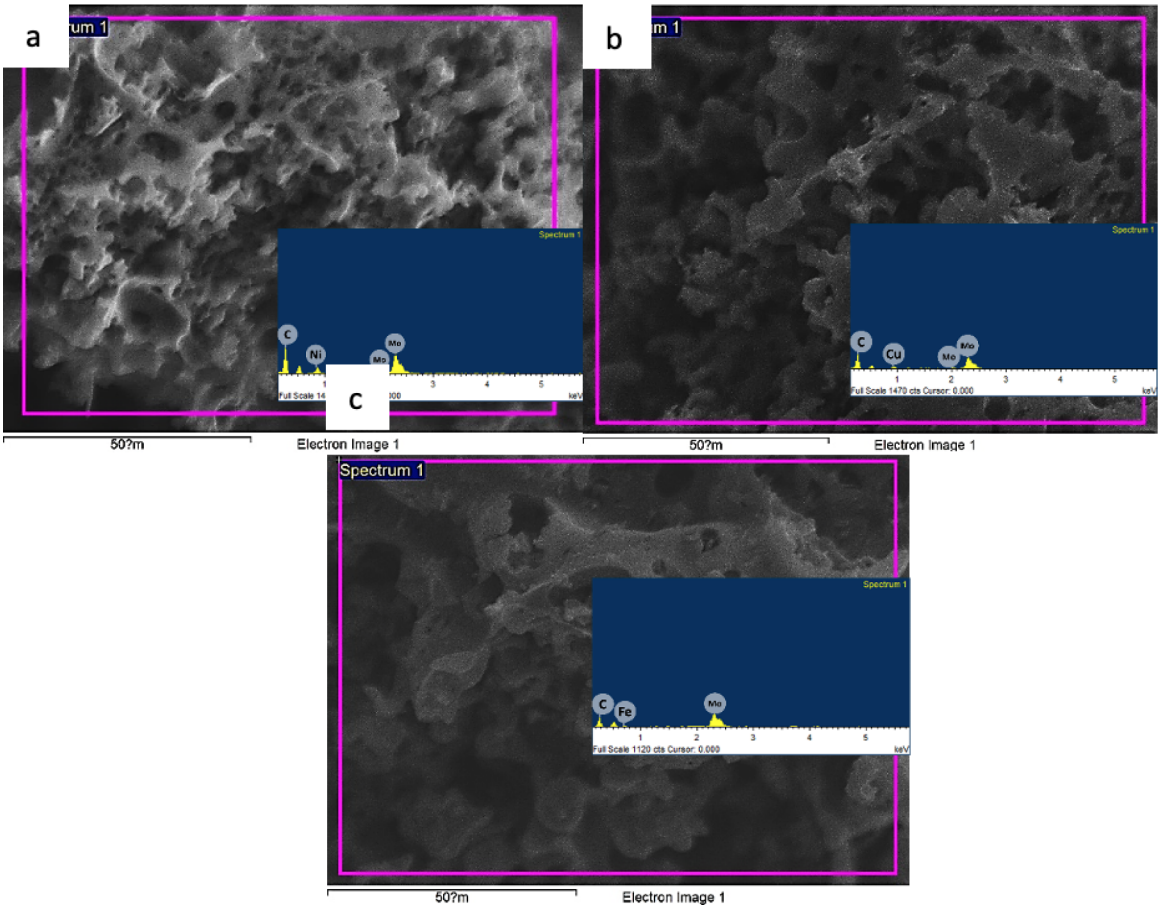

Figure 7. SEM images of the bimetallic (a) MoNi/NPC, (b) MoCu/NPC, and (c) MoFe/NPC catalysts.

strong band at 1600 and 860−724 cm^{-1}, which are attributed to the C═C stretching and C−H bending of aromatic in lignin. These results described that the cellulose structure was destroyed via dehydration, cracking, and partial polymerization reactions. The intensity of the hydroxyl group (−OH) and aliphatic alkane (−CH) was significantly reduced because cellulose was completely decomposed during physical activation above 700 °C. Meanwhile, the C═C stretching required an activation temperature up to 800 °C in destroying the lignin structure. Lignin was a complex structure with a decomposed temperature range of 300−800 °C. Therefore, lignin was destroyed when activated at 900 °C.[20]

The study of acid and alkaline activating agents was focused at 500 and 900 °C, respectively, because the acid activating agent was efficiently operated at 500 °C. On the other hand, an alkaline activating agent was operated at 900 °C. Table 2 shows the BET surface area, pore size, micropore volume (V_{micro}), mesopore volume (V_{meso}), and total pore volume (V_{total}) of nanoporous carbon treated with different activating agents (phosphoric acid (HP), sulfuric acid (HS), potassium hydroxide (KO) and sodium hydroxide (NO). Acid activation generated almost all micropores (<2 nm), while alkali activation highly promoted mesopores (2−50 nm).[21] According to the IUPAC classification, it is displayed in Figure 4. HP500−4 and HS500−4 samples were classified into type I, in which the characteristic of isotherm was consistent with a knee shape. These results explain that the amount of adsorption was rapidly enhanced at a low relative pressure of approximately 0.03, corresponding to the formation of a monolayer.[22] As a result, the gas molecules were rapidly filled to the wider micropores, while a small amount of gas absorbed in narrow mesopore that represented a hysteresis loop when the relative pressure was above 0.4. The acid activating agent acted as oxidizing agent which reacted on the surface of lignocellulose. The results indicated that HP500−4 had nearly doubled the BET surface area and total pore volume and HS500−4 because a dehydration of sulfuric acid provided excess water vaporization and low gasification of biomass.[23] Therefore, phosphoric acid seemed to be more effective on the surface reaction than sulfuric acid in promoting wider micropores with a surface area of 845.33 m^2g^{-1} and a pore size of 1.152 nm.

In comparison with alkaline activation, the shape of the adsorption isotherm was classified as type IV with a hysteresis loop, which indicated the mesopore volume. In this case, the adsorption of a gas molecule on the mesopore wall was initially monolayer-multilayer adsorption. The hysteresis loop indicated that the gas molecules were filled by a capillary condensation mechanism. The pore condensation was the phenomenon where gas condenses to a liquid-like phase within a pore at a pressure lower than P0 of the bulk liquid. This result indicated that the position of the curve of KO900−4 was higher than NO900−4 because KO900−4 has a larger surface area and pore size than NO900−4, corresponding to Table 1. Different atomic sizes of Na and K significantly affect the expansion of the pores, in which the atomic size of K (0.231 nm) is larger than that of Na (0.186 nm). This reason described the intercalation of the large K atom, which was mobile and stretchy in the gap of the graphene layer. Thus, the

https://doi.org/10.1021/acsomega.4c05207
ACS Omega 2024, 9, 42329−42342

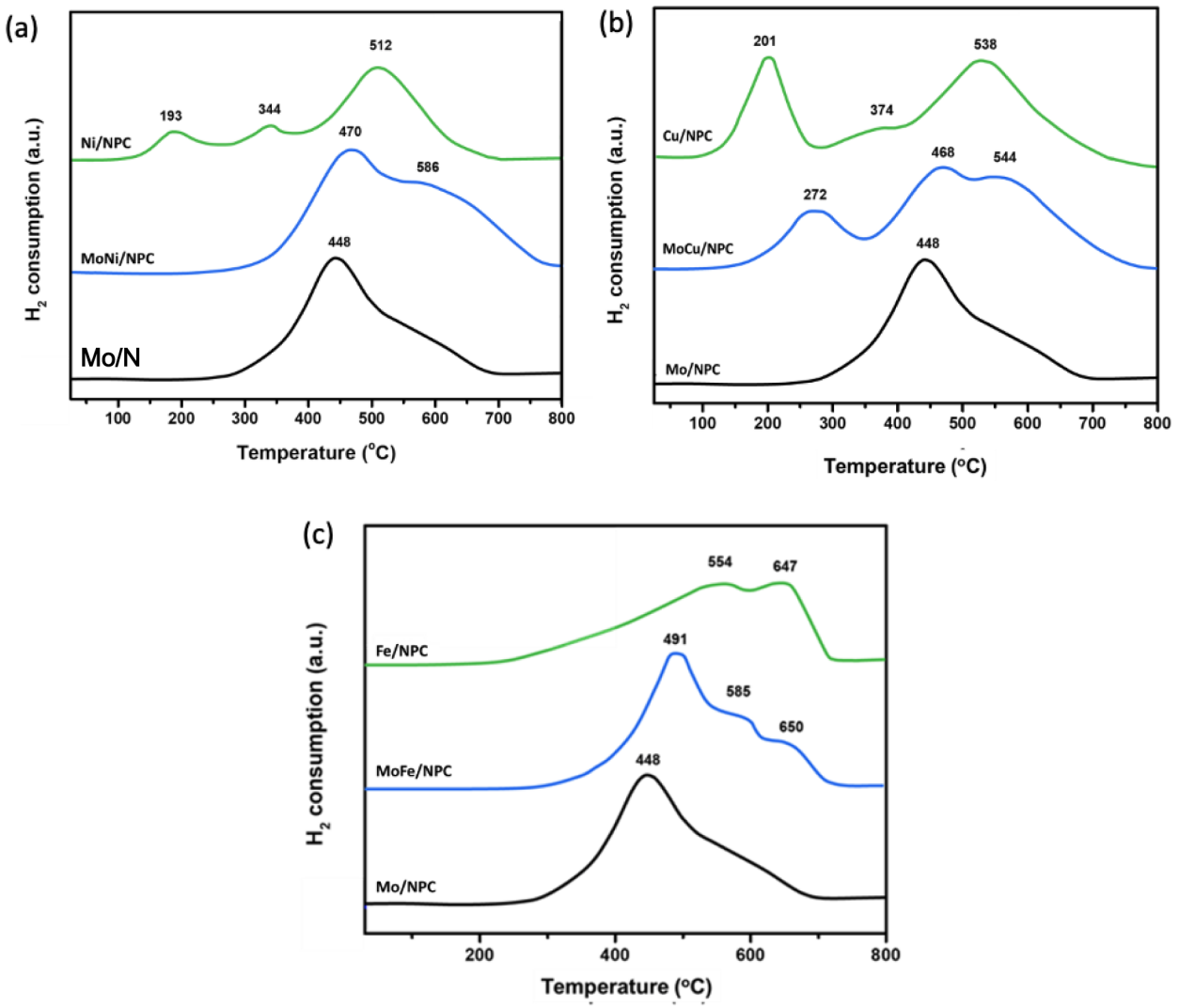

Figure 8. TPR-H_2 profiles of (a) Ni/NPC, MoNi/NPC, and Mo/NPC catalysts, (b) Cu/NPC, MoCu/NPC, and Mo/NPC catalysts, and (c) Fe/NPC, MoFe/NPC, and Mo/NPC catalysts.

expansion within pores by KOH was higher than that by NaOH activation. In contrast, the metallic Na slightly penetrated the lignocellulosic structure because it was appropriate to form the pore for the decomposition of precursors with a disorder structure such as sludge and residual.[24] The residual KOH, metallic K, salts, and impurity after the activation were eliminated by washing until neutralization was reached. Finally, the NPC was separated and dried to obtain high surface area carbon. KO900−4 has the maximum S_{BET} of 1323.5 m^2g^{-1}, while NaOH activation (NO900−4) created a S_{BET} of 1219.61 m^2g^{-1}. From the previous result, the alkaline activation was more advantageous than acid activation because it developed mesoporous material with connected pores.[25] In comparison with an alkaline activation, the shape of the adsorption isotherm was classified into type IV with a hysteresis loop, which indicated the mesopore volume. In this case, the adsorption of gas molecule on the mesopore wall was initially monolayer-multilayer adsorption. The hysteresis loop indicated that the gas molecules were filled by a capillary condensation mechanism. The pore condensation was the phenomenon that gas condensed to a liquid-like phase within a pore at lower than P_0 of the bulk liquid. This result indicated that the position of the curve of KO900−4 was higher than NO900−4 because KO900−4 has larger surface area and pore size than NO900−4, corresponding to Table 1. Different atomic sizes of Na and K significantly affect the expansion of the pores, in which the atomic size of K (0.231 nm) was larger than Na (0.186 nm). This reason described the intercalation of the large size K atom, which was mobile and stretchy in the gap of the graphene layer. Thus, the expansion within pores by KOH was higher than NaOH activation. Whereas the metallic Na slightly penetrated within the lignocellulosic structure because it was appropriate to form the pore for decomposition of precursors with disorder structure such as sludge and residual.[26] The residual KOH, metallic K, salts, and impurity after the activation were eliminated by washing until neutralization was reached. Finally, the NPC was separated and dried to obtain high surface area carbon. KO900−4 has the maximum S_{BET} of 1323.5 m^2g^{-1}, while NaOH activation (NO900−4) created a S_{BET} of 1219.61 m^2g^{-1}. From the previous result, alkaline activation was more advantageous than acid activation because it developed the microporous structure with connected pores.[27]

Figure 5 displays the morphologies of CL porous carbon observed using SEM. From Figure 5(a,b, raw CL and

https://doi.org/10.1021/acsomega.4c05207
ACS Omega 2024, 9, 42329−42342

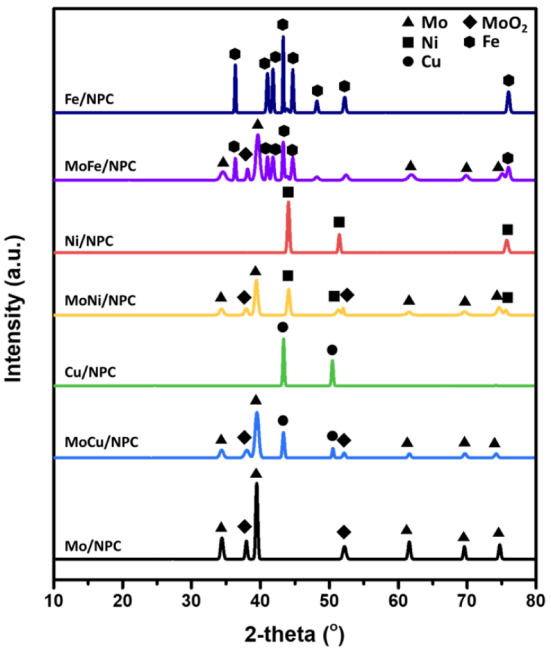

Figure 9. XRD patterns of Mo/NPC, MoCu/NPC, Cu/NPC, MoNi/NPC, Ni/NPC, MoFe/NPC, and Fe/NPC catalysts.

hydrothermal samples have a nonporous structure on the external surface. On the contrary, Figure 5c,d shows the surface morphology of HS500−4 and HP500−4, respectively. From Figure 5e,f, high-temperature carbonization combined with chemicals presents a lot of pores on the nanoporous carbon surface. In chemically treated lignocellulosic materials, the structure was well developed into porous carbon. This structure implies that the hemicellulose was significantly destroyed by high temperature, resulting in an improved porous surface structure. However, the sample obtained from the activation condition of 500 °C showed that such porous structures were likely to be formed during this process. These transformations indicated monomer decomposition and depolymerization of the component molecules such as carbohydrate components converted to spheres and porous carbons. HS500−4 shows a few pores because hemicellulose and lignin transformed to volatiles, while cellulose remained after chemical activation. HP500−4 revealed an irregular distribution of pores. Although the pores of HP500−4 were thoroughly dispersed on the surface, the internal solid was composed of closed pores. When comparing the NaOH and KOH activation, they generated connected pores within the carbon matrix as shown in Figure 5 e,f. These results describe that alkaline hydroxide activating agents release volatiles such as CO, CO_2, H_2, and H_2O. The obtained product led to the formation of small pores via dehydration and gasification reactions. Moreover, metal carbonate was reduced to metals, which were intercalated in the carbon layers and generated the connected pores. Apparently, the pore distribution of KO900−4 was more uniform than NO900−4 on both internal and external solids. Besides, the formation of pores also depends on the precursor with different structures and compositions. Consequently, KOH was favored for lignocellulose activation when compared to NaOH. From the previous results, KOH and H_3PO_4 are concluded to be good activating agents, having achieved the greatest micropore structure, respectively[26,28,29]

Moreover, the morphology of nanoporous carbon (KO500−4, KO700−4, and KO900−4) was obtained from 500−900 °C with potassium hydroxide, as shown in Figure 6. When reaching the activation temperature at 500 °C, KO500−4 gradually began to generate small pores on the external surface because the volatile matter was released from the char, which led to the development of diminutive pores on the external surface, as shown in Figure 6a. After that, the rise in temperature to 700 °C provided the diffusion of CO_2 or steam into the pores via simultaneous physical activation, which led to the extension of pores as observed in Figure 6b,c. It displayed a uniform pore distribution on the surface. The rising pore size emerged by the aggregation of the small pores. At 900 °C, metallic K intercalated within internal pores, which

Table 4. FAMEs Composition and Some Fuel Properties of Soybean FAMEs and Biodiesel Product After Reaction with Bimetallic Catalysts

FAMEs composition (%)	Soybean FAMEs	Soybean H-FAMEs			
	Feed	MoNi	MoCu	MoFe	Pd
C18:3 (wt %)	5.5	4.3	4.53	4.3	0.09
C18:2 (wt %)	52.2	42.5	47.18	48.5	0.04
C18:1 (wt %)	25.2	37.0	28.7	31.0	56.9
Trans (wt %)	0	1.9	1.93	0.9	20.1
Cis (wt %)	25.2	35.1	26.81	30.1	25.2
C18:0 (wt %)	4.1	4.1	6.39	4.2	29.4
Ratio trans/cis-C18:1	0	0.06	0.07	0.03	1.05
Conv. of C18:2 (%)	-	19.0	10.4	8.6	99.2
Cloud point (°C)	2	13	8	5	26
Pour point (°C)	−1	10	6	3	21
Oxidation stability (h)	2.4	14.6	8.2	6.7	40.3

Table 3. Characteristics of Catalysts

Catalyst	S_{BET}[a] (m^2g^{-1})	V_t[a] (cm^3g^{-1})	D_{av}[a] (nm)	Metal dispersion[b] (%)	Crystalline size of Mo[c] (nm)	Crystalline size of Ni[c] (nm)	Crystalline size of Cu[c] (nm)	Crystalline size of Fe[c] (nm)
Carbon	1323.58	0.78	2.78	-	-	-	-	-
Pd/NPC	403.32	0.51	2.31	48.45	-	-	-	-
Mo/NPC	343.80	0.37	1.72	39.92	12.17	-	-	-
Ni/NPC	307.63	0.42	1.89	36.07	-	15.62	-	-
Cu/NPC	92.64	0.14	0.87	10.56	-	-	41.02	-
Fe/NPC	53.10	0.11	0.74	6.43	-	-	-	39.89
MoNi/NPC	469.71	0.59	2.24	43.97	5.87	7.12	-	-
MoCu/NPC	154.28	0.27	1.12	18.88	8.62	-	25.43	-
MoFe/NPC	132.76	0.22	1.03	14.32	7.87	-	-	28.32

[a]Calculated by N_2 adsorption. [b]Calculated by H_2 chemisorption. [c]Calculated by X-ray diffraction.

https://doi.org/10.1021/acsomega.4c05207
ACS Omega 2024, 9, 42329−42342

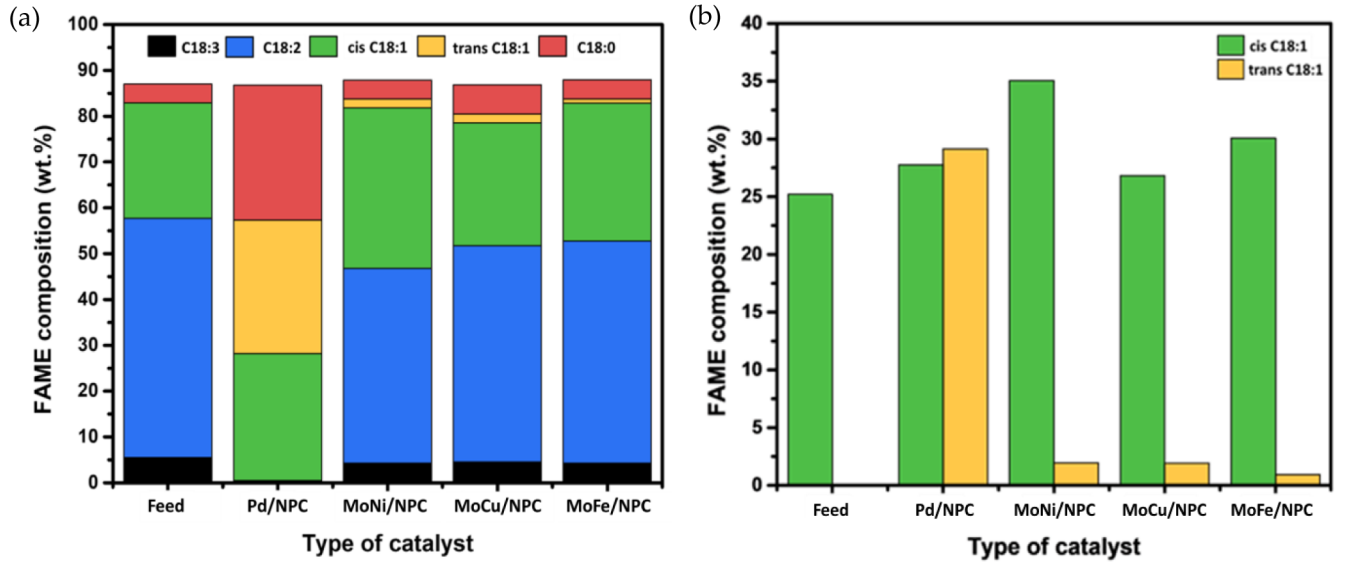

Figure 10. (a) Effect of bimetallic catalyst on the composition of C18, and (b) Effect of bimetallic catalyst on the composition of cis and trans C18:1 FAMEs.

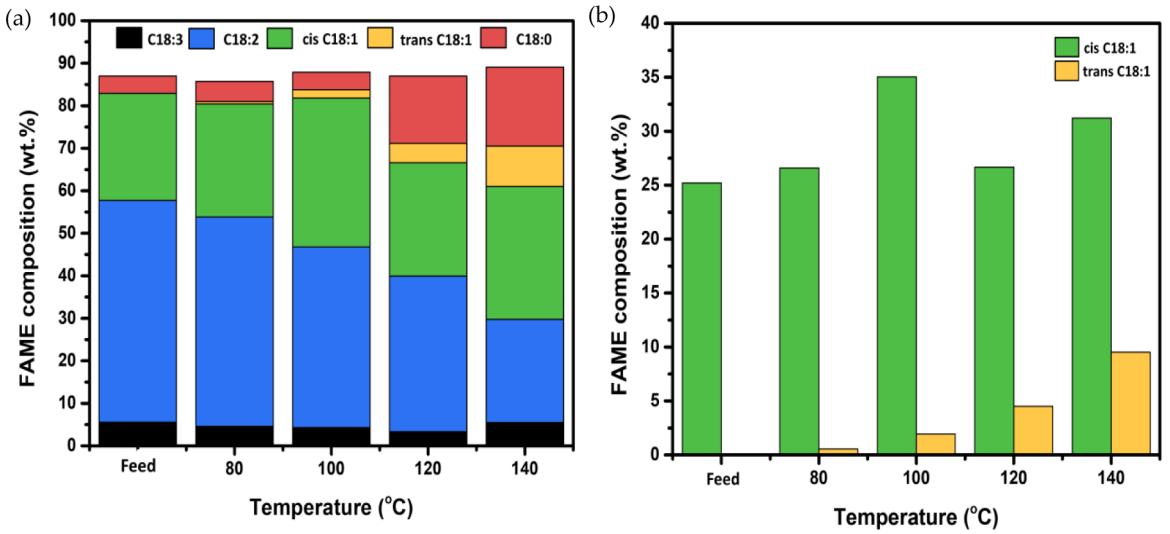

Figure 11. (a) Effect of reaction temperature on the composition of C18, and (b) Effect of reaction temperature on the composition of cis and trans C18:1 FAMEs.

formed a connected pore structure. KO900−4 exhibited that pores were completely linked throughout the bulk material.[30] These promoted the surface areas and diffusion of molecules into the inner structure. Therefore, the activation temperature at 900 °C significantly affected the formation of pores, indicating efficient activation by the KOH agents.

3.2. Characterization of Mono and Bimetallic Catalysts Supported on NPC. The studied catalysts, including Pd/NPC, Mo/NPC, Ni/NPC, Cu/NPC, Fe/NPC, MoNi/NPC, MoCu/NPC, and MoFe/NPC were synthesized via a wet impregnation technique. The catalysts were analyzed using EDX, H_2-TPR, XRD, TEM, BET, and H_2 chemisorption to elucidate the catalyst properties. The surface morphology and elemental composition of the catalyst were investigated using a scanning electron microscope and energy dispersive spectroscopy. Figure 7 shows the presence of bimetallic (a) MoNi/NPC, (b) MoCu/NPC, and (c) MoFe/NPC catalysts, which confirms the elemental content from the EDS analysis.

Moreover, Figure 8 shows that the reducibility of catalysts analyzed using a hydrogen temperature-programmed reduction technique. Figure 8a reveals the H_2-TPR profiles of the Ni/NPC, MoNi/NPC, and Mo/NPC catalysts. The H_2-TPR profiles of the Ni/NPC catalyst presented three reduction bands at 193, 344, and 512 °C, which indicated the reduction of metal oxide to metallic Ni. The bulk NiO was reduced at temperatures lower than 350 °C, while the strong interaction of NiO on the support was further reduced above 512 °C to generate metallic Ni. The reduction temperature of the Mo/NPC catalyst at around 448 °C is assigned to the reduction temperature of Mo oxide. The TPR profile of the MoNi/NPC catalyst shows two broad peaks, which overlap at 470 and 562 °C. For the initial step, the weak interaction of octahedral molybdenum (Mo^{6+}) with the support was easily reduced to tetrahedral molybdenum (Mo^{5+}). Hence, the reduction of MoO_3 to Mo metal is presented as follows:

$$2MoO_3 + H_2 = Mo_2O_5 + H_2O \quad (1)$$

https://doi.org/10.1021/acsomega.4c05207
ACS Omega 2024, 9, 42329−42342

Table 5. FAME Composition and Some Fuel Properties of Soybean FAMEs and Biodiesel Product after Reaction with the MoNi/NPC Catalyst

FAMEs composition (%)	Soybean FAMEs	Soybean H-FAMEs			
	Feed	80 °C	100 °C	120 °C	140 °C
C18:3 (wt %)	5.3	4.6	4.3	3.3	1.7
C18:2 (wt %)	52.2	49.2	42.5	36.6	24.3
C18:1 (wt %)	25.2	27.1	37.0	31.2	40.7
trans	0	0.5	1.9	4.5	9.5
cis	25.2	26.6	35.1	26.7	31.2
C18:0	4.1	4.6	4.1	15.8	18.5
ratio trans/cis-C18:1	-	0.02	0.06	0.17	0.30
Conv. of C18:2	-	6.8	19.0	30.8	87.6
CP	2	4	13	15	25
PP	−1	1	10	11	20
Oxidation stability	2.4	4.1	14.6	19.4	30.6

$$Mo_2O_5 + H_2 = 2MoO2 + H_2O \quad (2)$$

$$MoO_2 + 2H_2 = Mo + H_2O \quad (3)$$

Moreover, the weaker peak at 570 °C indicated the reduction of Ni^{2+} to metallic Ni. The Ni species were more dominant in comparison to Mo^{4+} species because Mo^{4+} required a higher temperature (>800 °C) for the formation of Mo0 species on the support. The position of the Mo peak shifted to the higher temperature (448 to 470 °C) in comparison to the Mo/NPC due to the interaction between Mo and Ni species.[31] Besides, the secondary peak of Ni shifts to the higher temperature (512 to 586 °C), which demonstrates stronger interaction of metallic Ni with the support.[32] These results confirmed that the MoNi/NPC catalyst exhibited the higher interaction between metal and support.

Figure 8b shows the TPR profiles of Cu/NPC, MoCu/NPC, and Mo/NPC. The TPR profiles of the Cu/NPC catalyst illustrate three different peaks located at 201, 374, and 538 °C. The first peak in the temperature range of 100−280 °C is attributed to the reduction of CuO species, as Cu^{2+} transformed to Cu^{1+}. Above 400 °C, the intermediate Cu^{1+} was completely reduced to metallic Cu, which exhibited at the terminal peak. The reduction temperature of metallic Cu was higher compared to metallic Ni because metallic Cu favored agglomeration to large particles on the support. The peaks of Mo and Cu in the MoCu/NPC catalyst overlapped in the temperature range of 400−600 °C. The peak of metallic Cu reduction shifted to a higher temperature, indicating the interaction between the metal and the support. It was described that the agglomeration of Cu clusters decreased, because the formation of Mo metal reduced the crystallite size of Cu. On the other hand, the position of the Mo peak in the MoCu/NPC catalyst rarely changed when compared with the Mo/NPC and Cu/NPC catalysts.[33]

Figure 8c displays the TPR profiles of the Fe/NPC, MoFe/NPC, and Mo/NPC catalysts. The TPR profiles of the Fe/NPC catalyst revealed two peaks at 554 and 647 °C. The first peak (554 °C) is attributed to the reduction of Fe_3O_4 to FeO, while the last peak (647 °C) is ascribed to the reduction of FeO to metallic Fe. The reduction temperature of Fe metal was higher than that of Ni and Cu metals because of the large grain size of Fe. The peaks of Mo and Fe in the MoFe/NPC catalyst overlapped in the temperature range of 450−700 °C. The reduction temperature of the MoFe/NPC catalyst was slightly increased compared to the Fe/NPC catalyst because of the stronger interaction of Mo and Fe on the support.[34]

The formation of metal catalysts was identified in the 2θ range of 10−80° by X-ray diffraction. Figure 9 reveals the XRD patterns of Mo/NPC, MoCu/NPC, Cu/NPC, MoNi/NPC, Ni/NPC, MoFe/NPC, and Fe/NPC catalysts. No diffraction peaks of carbon were observed in all samples because the amorphous structure of the carbon support exhibits a very broad peak characteristic with extremely low intensity when compared with those of metal sites. The peaks of Mo metal appeared at 34.74°, 39.15°, 62.32°, 69.89°, and 74.88°, with the highest intensity of Mo indicated to be (111). Moreover, the peaks of MoO_2 are observed at 41.65°, 38.86°, and 53.54° because MoO_2 requires a reduction temperature above 1000 °C to form Mo metallic. The peaks of Ni metal at 44.78°, 52.36°, and 74.12° corresponded to (111), (220), and (200) planes, respectively, while the peaks of Cu at 43.05° and 51.29° represented (111) and (200) planes, respectively. The XRD pattern of Fe metal exhibited peaks at 35.28°, 41.07°, 42.11°, 44.24°, 45.02°, 48.39°, 53.39°, and 76.21°, at which the highest intensity of Fe was attributed to the (110) plane. Furthermore, the reduction of crystallinity in bimetallic catalysts decreased the intensity of the peaks.

The crystalline size was evaluated using the Debye−Scherrer equation in Table 3. The crystallite size of the bimetallic catalysts (MoNi, MoCu, and MoFe) was smaller than that of the monometallic catalysts because the growth of grain size was interrupted by Mo metallic. The Mo catalyst has the smallest crystallite size of 12.17 nm compared to Ni, Cu, and Fe because of the high dispersion of Mo on the carbon support of about 36.07% from the H_2 chemisorption technique. On the contrary, the crystallite size of Fe and Cu catalysts significantly increased to 39.89 and 41.02 nm, respectively, because Fe and Cu particles highly agglomerated on the support. Moreover, Cu and Fe metals, as large particles blocked within pores, which contributed to low surface area and low metal dispersion. This could be explained by the fact that the increase in crystallite size was associated with the increase in the particle size.

Table 3 exhibits these parameters for the investigation of catalysts after reduction of metal. The N_2 adsorption techniques indicate that the surface properties (S_{BET}, V_{total}, and D_{avg}) of the catalyst were reduced when compared with those of the support as the metal dispersions (%) were inspected by H_2 chemisorption. The decrease in porosity can be described by an increase in metal dispersion (%) within pores. When considering a bimetallic catalyst, the surface area (S_{BET}), pore volume (V_{total}), and pore size (D_{avg}) of the MoNi/NPC catalyst increased to 469.71 m^2g^{-1}, 0.59 cm^3g^{-1}, and 2.24 nm, respectively, which provided a metal dispersion of 43.97%. The results described that Mo significantly decreased the particle size of Ni. In contrast, MoCu/NPC and MoFe/NPC catalysts with pore sizes smaller than 2 nm have a low metal dispersion of 18.44% and 14.32%. Therefore, the metal dispersion of molybdenum-based catalysts was in the order as follows: MoNi > MoCu > MoFe. However, the specific properties of the MoNi/NPC catalyst, such as textural pore characteristics and %metal dispersion, were consistent with the Pd/NPC catalyst. This could imply that the MoNi/NPC catalyst could have a superior catalyst activity, as well as

https://doi.org/10.1021/acsomega.4c05207
ACS Omega 2024, 9, 42329−42342

supported Pd catalysts during the partial hydrogenation of soybean oil.

From the synthesis of the molybdenum-based catalysts on carbon support via wet impregnation, the presence of metal particles with a crystalline structure on the carbon support has been achieved. The metal dispersion, surface area, and pore size of the Mo-based catalyst increased in comparison with other monometallic catalysts. In contrast, the reduction of the crystallite size provided a decrease in the particle size. The Mo-based catalyst significantly affects the catalyst properties and the performance. Thus, the activity of the catalyst would be further investigated in partial hydrogenation.

3.3. Reaction Study in Partial Hydrogenation Process.

The catalytic activity for partial hydrogenation of soybean FAMEs was investigated to improve the fuel properties, such as oxidation stability, cloud point, and pour point. The as-prepared catalysts were investigated for their catalytic performance (i.e., conversion of polyunsaturated FAMEs, selectivity of cis C18:1) compared with the Pd/NPC catalyst at various reaction temperature conditions.

The limitations of monometallic catalysts involved low activity and selectivity of the cis-isomer content in hydrogenated biodiesel. In this part, the second metals were added to modify the formation of trans C18:1 in the Mo catalyst. The partial hydrogenation of biodiesel was operated at 100 °C, 0.4 bar, and 100 mL/min of hydrogen flow rate using bimetallic catalysts (MoNi/NPC, MoCu/NPC, and MoFe/NPC), which promoted Mo metal using various second metals. Mo promoted the adsorption of H_2 after the hydrogenation reaction on the Ni, Cu, and Fe surfaces. As shown in Table 4, the MoNi/NPC catalyst in Figure 10 exhibited high catalytic activity with an increase in polyunsaturated content, because the Ni active site limited the catalytic activity of Mo due to large particle size and low metal dispersion. Although the Pd/NPC catalyst exhibited the highest activity under mild conditions, the conversion of C18:3 and C18:2 derived the product with selectivity toward C18:0 and trans-isomers. The high amount of C18:0 provided a negative impact on the poor cold flow properties of.[35] Therefore, the product hydrogenated by the MoNi/NPC catalyst improved the oxidation stability while maintaining satisfactory cold flow properties.

The effect of temperature was examined using a MoNi/NPC catalyst at 0.4 bar, H_2 flow rate of 100 mL/min, and a FAME flow rate of 40 g/h. As exhibited in Figure 11, the effects of the reaction temperature on the catalytic activity,cis-C18:1 selectivity ratio, and fuel properties varied from 80 to 140 °C. Table 5 indicated that the conversion of C18:2 and C18:3 at 80, 100, 120, and 140 °C was 6.78%, 17.29%, 35.68%, and 54.78%, respectively. Although an increase in the reaction temperature improved the conversion of C18:2 and C18:3, the low-temperature flow properties worsened. Above 120 °C, the cis C18:1 was rapidly converted to trans-C18:1 and C18:0, which increased the cloud point and pour point while compromising oxidation stability.[12,36,37] The high reaction temperature significantly influenced the isomerization of cis C18:1 because the faster reaction rate provided a high mobility and collisions of molecules according to kinetics principle. In contrast, the formation of trans C18:1 and C18:0 at 80 and 100 °C was due to the low isomerization reaction. Therefore, the reaction temperature of 100 °C was optimal in improving the fuel properties of soybean biodiesel, in which the oxidation stability was significantly elevated from 2.37 to 14.56 h. Moreover, the increase of cis-unsaturated FAMEs improved the cloud point and pour point from 2 to 13 °C and from −1 to 10 °C.

4. CONCLUSIONS

The synthesis of nanoporous carbon (NPC) from cattail leaves (CL) via hydrothermal carbonization with chemical activation using different activating agents (KOH, NaOH, H_3PO_4, and H_2SO_4) was investigated to produce high surface area carbon support. The activation temperature shows a more influential effect on nanoporous carbon properties than the concentration of the activating agents. The nanoporous carbon with a surface area of 1324 m^2/g was obtained from KOH activation at a concentration of 4 M and 900 °C. The prepared NPC indicated a high carbon content of 81.18% with low ash content. Moreover, it was classified as a mesopore with a pore size of 2.24 nm. Then, the NPC was used as a catalyst support for the partial hydrogenation reaction. The molybdenum-based catalysts (MoNi, MoCu, and MoFe) were impregnated on nanoporous carbon (NPC) using a rotary evaporation technique. The microscopic analysis revealed the uniform distribution of MoNi nanoparticles with a 7.2 nm particle size. The surface area and pore size decreased from 1323.58 to 469.71 m^2/g and 2.78 to 2.24 nm, respectively, after impregnation with 5:5 wt % of MoNi/NPC catalyst. The XRD results exhibited no alloy phase formation between Mo and Ni in the MoNi/NPC catalyst with Mo crystallite size of 5.87 nm and Ni crystallite size of 7.12 nm. Furthermore, the MoNi/NPC catalyst comprised43.97% of metal dispersion using H_2 chemisorption, which improved the activity of partial hydrogenation. The results confirmed that the MoNi/NPC catalyst was favorable in partial hydrogenation for improving the oxidation stability and cold flow properties of soybean biodiesel. The MoNi/NPC catalyst showed superior catalytic activity and selectivity of cis-C18:1 compared to those of the other bimetallic catalysts and the Pd/NPC catalyst. Besides, the reaction temperature of 100 °C increased polyunsaturated FAMEs, trans-C18:1, and C18:0 to 18%, 1.94%, and 4.14%, respectively. The MoNi/NPC catalyst escalated the oxidation stability from 3 to 14 h, while the cloud point and pour point increased from 2 to 13 °C and from −1 to 10 °C, respectively. The partially hydrogenated biodiesel was therefore able to be stored for a longer period according to US ASTM D6751 and EU EN14214 standards.

■ ASSOCIATED CONTENT

Data Availability Statement

All data generated or analyzed during this study are included in this published article.

■ AUTHOR INFORMATION

Corresponding Author

Apiluck Eiad-Ua − *College of Materials Innovation and Technology, King Mongkut's Institute of Technology Ladkrabang, Bangkok, Ladkrabang 10520, Thailand*; Phone: +66−2−329−8300 ext. 3132; Email: apiluck.ei@kmitl.ac.th; Fax: +66−2−329−8625

Authors

Dolrudee Jaruwat − *Center of Excellence in Catalysis and Catalytic Reaction Engineering, Department of Chemical Engineering, Faculty of Engineering, Chulalongkorn University, Bangkok 10330, Thailand*

https://doi.org/10.1021/acsomega.4c05207
ACS Omega 2024, 9, 42329−42342

Napat Kaewtrakulchai − *Kasetsart Agricultural and Agro-Industrial Product Improvement Institute, Kasetsart University, Bangkok, Bangkhen 10900, Thailand*
Siwat Siriorarnroj − *Center of Excellence in Catalysis and Catalytic Reaction Engineering, Department of Chemical Engineering, Faculty of Engineering, Chulalongkorn University, Bangkok 10330, Thailand*
Atthapon Srifa − *Department of Chemical Engineering, Faculty of Engineering, Mahidol University, Nakhon Pathom 73170, Thailand;* orcid.org/0000-0002-9593-5014
Worapon Kiatkittipong − *Department of Chemical Engineering, Faculty of Engineering and Industrial Technology, Silpakorn University, Nakhon Pathom 73000, Thailand*
Sumittra Charojrochkul − *National Energy Technology Center, Thailand Science Park, Pathumthani 12120, Thailand*
Masayoshi Fuji − *Advanced Ceramic Center, Nagoya Institute of Technology, Gifu 466-8555, Japan*
Suttichai Assabumrungrat − *Center of Excellence in Catalysis and Catalytic Reaction Engineering, Department of Chemical Engineering, Faculty of Engineering, Chulalongkorn University, Bangkok 10330, Thailand; Bio-Circular-Green-economy Technology & Engineering Center, BCGeTEC, Department of Chemical Engineering, Faculty of Engineering, Chulalongkorn University, Bangkok 10330, Thailand*

Complete contact information is available at: https://pubs.acs.org/10.1021/acsomega.4c05207

Author Contributions

N.K. and A.E. contributed to conceptualization; D.J. contributed to methodology; A.S., W.K., and S.C. contributed to validation; D.J., S.S., and N.K. contributed to formal analysis; D.J. and A.E. contributed to investigation ; A.E. and S.A. contributed to supervision; D.J. contributed to writing−original draft; S.A. and A.E. contributed to writing−review and editing. All authors have read and agreed to the published version of the manuscript.

Funding

This research received no external funding

Notes

The authors declare no competing financial interest.

■ ACKNOWLEDGMENTS

The authors acknowledge the Center of Excellence on Catalysis and Catalytic Reaction Engineering, College of Materials Innovation and Technology, King Mongkut's Institute of Technology Ladkrabang, and the National Energy Technology Center, National Science and Technology Development Agency for their facility and financial support.

■ REFERENCES

(1) Alagumalai, A.; Mahian, O.; Hollmann, F.; Zhang, W. Environmentally benign solid catalysts for sustainable biodiesel production: A critical review. *Sci. Total Environ.* **2021**, *768*, 144856.
(2) Habibullah, M.; Masjuki, H. H.; Kalam, M. A.; Rahman, S. M. A.; Mofijur, M.; Mobarak, H. M.; Ashraful, A. M. Potential of biodiesel as a renewable energy source in Bangladesh. *Renewable Sustainable Energy Rev.* **2015**, *50*, 819−834.
(3) Mofijur, M.; Rasul, M. G.; Hyde, J.; Azad, A. K.; Mamat, R.; Bhuiya, M. M. K. Role of biofuel and their binary (diesel−biodiesel) and ternary (ethanol−biodiesel−diesel) blends on internal combustion engines emission reduction. *Renewable Sustainable Energy Rev.* **2016**, *53*, 265−278.
(4) Bastos, R. R. C.; da Luz Corrêa, A. P.; da Luzda Luz, P. T. S.; da Rocha Filho, G. N.; Zamian, J. R.; da Conceição, L. R. V. Optimization of biodiesel production using sulfonated carbon-based catalyst from an amazon agro-industrial waste. *Energy Convers. Manage.* **2020**, *205*, 112457.
(5) Cao, M.; Peng, L.; Xie, Q.; Xing, K.; Lu, M.; Ji, J. Sulfonated Sargassum horneri carbon as solid acid catalyst to produce biodiesel via esterification. *Bioresour. Technol.* **2021**, *324*, 124614.
(6) Degfie, T. A.; Mamo, T. T.; Mekonnen, Y. S. Optimized Biodiesel Production from Waste Cooking Oil (WCO) using Calcium Oxide (CaO) Nano-catalyst. *Sci. Rep.* **2019**, *9*, 18982.
(7) Lathiya, D. R.; Bhatt, D. V.; Maheria, K. C. Synthesis of sulfonated carbon catalyst from waste orange peel for cost effective biodiesel production. *Bioresour. Technol. Rep.* **2018**, *2*, 69−76.
(8) Mahmudul, H. M.; Hagos, F. Y.; Mamat, R.; Adam, A. A.; Ishak, W. F. W.; Alenezi, R. Production, characterization and performance of biodiesel as an alternative fuel in diesel engines − A review. *Renewable Sustainable Energy Rev.* **2017**, *72*, 497−509.
(9) Rocha, P. D.; Oliveira, L. S.; Franca, A. S. Sulfonated activated carbon from corn cobs as heterogeneous catalysts for biodiesel production using microwave-assisted transesterification. *Renewable Energy* **2019**, *143*, 1710−1716.
(10) Zailan, Z.; Tahir, M.; Jusoh, M.; Zakaria, Z. Y. A review of sulfonic group bearing porous carbon catalyst for biodiesel production. *Renewable Energy* **2021**, *175*, 430−452.
(11) Du, L.; Li, Z.; Ding, S.; Chen, C.; Qu, S.; Yi, W.; Lu, J.; Ding, J. Synthesis and characterization of carbon-based MgO catalysts for biodiesel production from castor oil. *Fuel* **2019**, *258*, 116122.
(12) Tang, Z.-E.; Lim, S.; Pang, Y.-L.; Shuit, S.-H.; Ong, H.-C. Utilisation of biomass wastes based activated carbon supported heterogeneous acid catalyst for biodiesel production. *Renewable Energy* **2020**, *158*, 91−102.
(13) Başakçılardan Kabakcı, S.; Baran, S. S. Hydrothermal carbonization of various lignocellulosics: Fuel characteristics of hydrochars and surface characteristics of activated hydrochars. *Waste Manage.* **2019**, *100*, 259−268.
(14) Wilk, M.; Magdziarz, A.; Jayaraman, K.; Szymańska-Chargot, M.; Gökalp, I. Hydrothermal carbonization characteristics of sewage sludge and lignocellulosic biomass. A comparative study. *Biomass Bioenergy* **2019**, *120*, 166−175.
(15) Jaruwat, D.; Udomsap, P.; Chollacoop, N.; Fuji, M.; Eiad-ua, A. Effects of hydrothermal temperature and time of hydrochar from Cattail leaves. *AIP Conf. Proc.* **2018**, *2010*, 020016.
(16) Wang, L.; Guo, Y.; Zou, B.; Rong, C.; Ma, X.; Qu, Y.; Li, Y.; Wang, Z. High surface area porous carbons prepared from hydrochars by phosphoric acid activation. *Bioresour. Technol.* **2011**, *102*, 1947−1950.
(17) Yakout, S. M.; Sharaf El-Deen, G. Characterization of activated carbon prepared by phosphoric acid activation of olive stones. *Arabian J. Chem.* **2016**, *9*, S1155−S1162.
(18) Narowska, B.; Kułażyński, M.; Łukaszewicz, M.; Burchacka, E. Use of activated carbons as catalyst supports for biodiesel production. *Renewable Energy* **2019**, *135*, 176−185.
(19) Nayebzadeh, H.; Haghighi, M.; Saghatoleslami, N.; Tabasizadeh, M.; Yousefi, S. Fabrication of carbonated alumina doped by calcium oxide via microwave combustion method used as nanocatalyst in biodiesel production: Influence of carbon source type. *Energy Convers. Manage.* **2018**, *171*, 566−575.
(20) Balajii, M.; Niju, S. A novel biobased heterogeneous catalyst derived from Musa acuminata peduncle for biodiesel production − Process optimization using central composite design. *Energy Convers. Manage.* **2019**, *189*, 118−131.
(21) Jamil, F.; Kumar, P. S. M.; Al-Haj, L.; Myint, M. T. Z.; Al-Muhtaseb, A. H. Heterogeneous carbon-based catalyst modified by alkaline earth metal oxides for biodiesel production: Parametric and kinetic study. *Energy Convers. Manage.* **2021**, *10*, 100047.

(22) Al-Muhtaseb, A. H.; Jamil, F.; Al-Haj, L.; Zar Myint, M. T.; Mahmoud, E.; Ahmad, M. N. M.; Hasan, A. O.; Rafiq, S. Biodiesel production over a catalyst prepared from biomass-derived waste date pits. *Biotechnol. Rep.* **2018**, *20*, No. e00284.
(23) Chai, I. V. K.; Lim, X. Y.; Lee, T. Creatinine adsorption by activated carbon fibre (ACF) derived from empty fruit bunch (EFB) fibre. *J. Eng. Sci. Technol.* **2017**, *12*, 58−70.
(24) Namazi, A.; Allen, D. G.; Jia, C. Q. Benefits of microwave heating method in production of activated carbon. *Can. J. Chem. Eng.* **2016**, *94*, 1262−1268.
(25) Raymundo-Piñero, E.; Azaïs, P.; Cacciaguerra, T.; Cazorla-Amorós, D.; Linares-Solano, A.; Béguin, F. KOH and NaOH activation mechanisms of multiwalled carbon nanotubes with different structural organisation. *Carbon* **2005**, *43*, 786−795.
(26) Wong, W. Y.; Lim, S.; Pang, Y. L.; Shuit, S. H.; Chen, W. H.; Lee, K. T. Synthesis of renewable heterogeneous acid catalyst from oil palm empty fruit bunch for glycerol-free biodiesel production. *Sci. Total Environ.* **2020**, *727*, 138534.
(27) Ayoob, A. K.; Fadhil, A. B. Biodiesel production through transesterification of a mixture of non-edible oils over lithium supported on activated carbon derived from scrap tires. *Energy Convers. Manage.* **2019**, *201*, 112149.
(28) Saravanan Arumugamurthy, S.; Sivanandi, P.; Pandian, S.; Choksi, H.; Subramanian, D. Conversion of a low value industrial waste into biodiesel using a catalyst derived from brewery waste: An activation and deactivation kinetic study. *Waste Manage.* **2019**, *100*, 318−326.
(29) Shobhana-Gnanaserkhar; Asikin-Mijan, N.; AbdulKareem-Alsultan, G.; Sivasangar, S.; Izham, S. M.; Taufiq-Yap, Y. H. Biodiesel production via simultaneous esterification and transesterification of chicken fat oil by mesoporous sulfated Ce supported activated carbon. *Biomass Bioenergy* **2020**, *141*, 105714.
(30) Lan, X.; Jiang, X.; Song, Y.; Jing, X.; Xing, X. The effect of activation temperature on structure and properties of blue coke-based activated carbon by CO2 activation. *Green Process. Synth.* **2019**, *8*, 837−845.
(31) Le, M. C.; Van, K. L.; Nguyen, T. H. T.; Nguyen, N. H. The Impact of Ce-Zr Addition on Nickel Dispersion and Catalytic Behavior for CO_2 Methanation of Ni/AC Catalyst at Low Temperature. *J. Chem.* **2017**, *2017*, 4361056.
(32) Yin, H.; Zhou, T.; Liu, Y.; Chai, Y.; Liu, C. NiMo/Al2O3 catalyst containing nano-sized zeolite Y for deep hydrodesulfurization and hydrodenitrogenation of diesel. *J. Nat. Gas Chem.* **2011**, *20*, 441−448.
(33) Golub, K. W.; Sulmonetti, T. P.; Darunte, L. A.; Shealy, M. S.; Jones, C. W. Metal−Organic-Framework-Derived Co/Cu−Carbon Nanoparticle Catalysts for Furfural Hydrogenation. *ACS Appl. Nano Mater.* **2019**, *2*, 6040−6056.
(34) Chen, S.; Jang, H.; Wang, J.; Qin, Q.; Liu, X.; Cho, J. Bimetallic metal-organic framework-derived MoFe-PC microspheres for electrocatalytic ammonia synthesis under ambient conditions. *J. Mater. Chem. A* **2020**, *8*, 2099−2104.
(35) Naeem, M. M.; Al-Sakkari, E. G.; Boffito, D. C.; Gadalla, M. A.; Ashour, F. H. One-pot conversion of highly acidic waste cooking oil into biodiesel over a novel bio-based bi-functional catalyst. *Fuel* **2021**, *283*, 118914.
(36) Mohamed, R. M.; Kadry, G. A.; Abdel-Samad, H. A.; Awad, M. E. High operative heterogeneous catalyst in biodiesel production from waste cooking oil. *Egypt. J. Pet.* **2020**, *29*, 59−65.
(37) Tang, Z.-E.; Lim, S.; Pang, Y.-L.; Ong, H.-C.; Lee, K.-T. Synthesis of biomass as heterogeneous catalyst for application in biodiesel production: State of the art and fundamental review. *Renewable Sustainable Energy Rev.* **2018**, *92*, 235−253.

https://doi.org/10.1021/acsomega.4c05207
ACS Omega 2024, 9, 42329−42342